Tuning of Jahn-Teller distortions via sterically enforced lattice enlargement of Cu(ta)2-type coordination polymers

Marcel Hirrle, Richard Röß-Ohlenroth, Stephan Reschke, Björn Bredenkötter, Hans-Albrecht Krug von Nidda, Dirk Volkmer

Angaben zur Veröffentlichung / Publication details:

Hirrle, Marcel, Richard Röß-Ohlenroth, Stephan Reschke, Björn Bredenkötter, Hans-Albrecht Krug von Nidda, and Dirk Volkmer. 2026. "Tuning of Jahn-Teller distortions via sterically enforced lattice enlargement of Cu(ta)2-type coordination polymers." *Journal of Physics and Chemistry of Solids* 212: 113566. https://doi.org/10.1016/j.jpcs.2026.113566.

Journal of Physics and Chemistry of Solids 212 (2026) 113566

Contents lists available at ScienceDirect

Journal of Physics and Chemistry of Solids

journal homepage: www.elsevier.com/locate/jpcs

Tuning of Jahn-Teller distortions via sterically enforced lattice enlargement of $Cu(ta)_2$-type coordination polymers☆

Marcel Hirrle [a], Richard Röß-Ohlenroth [a], Stephan Reschke [b], Björn Bredenkötter [a], Hans-Albrecht Krug von Nidda [b], Dirk Volkmer [a,*]

[a] Chair of Solid State and Materials Chemistry, Institute of Physics, University of Augsburg, Universitätsstraße 1, D-86159, Augsburg, Germany
[b] Experimental Physics V, Center for Electronic Correlations and Magnetism, Institute of Physics, University of Augsburg, Universitätsstraße 1, D-86159, Augsburg, Germany

A B S T R A C T

The control of Jahn-Teller distortions in copper-based coordination polymers is crucial for tuning their magnetic and structural properties. Here, we report the synthesis and characterization of two novel Cu(II)-based metal-organic frameworks (MOFs), $Cu(mta)_2$ and $Cu(cta)_2$, derived from modified triazole ligands. By introducing steric bulk through methyl and cyclopentyl substituents, we systematically investigate the effect of lattice enlargement on local coordination environments and magnetic behaviour.

Single-crystal and powder X-ray diffraction analyses reveal that $Cu(mta)_2$ exhibits static Jahn-Teller distortions similar to those observed in $Cu(ta)_2$, whereas $Cu(cta)_2$ crystallizes in an undistorted, near-ideal cubic structure. Magnetic susceptibility and electron spin resonance measurements show strong antiferromagnetic interactions and temperature-dependent g-factor anisotropy for $Cu(ta)_2$ and $Cu(mta)_2$, while $Cu(cta)_2$ displays nearly isotropic magnetic behavior and only dynamically JT distortions without a cooperative phase transition.

These results demonstrate that steric ligand design offers a powerful strategy to modulate the interplay between lattice structure and magnetic anisotropy. Our findings provide fundamental insights into the suppression of cooperative static Jahn-Teller distortions and open pathways for the targeted design of multifunctional MOFs with tailored structural and magnetic properties.

1. Introduction

The versatile structural architectures and tunable porosity of metal-organic frameworks (MOFs) offer a compelling platform for the incorporation of magnetic properties [1]. As hybrid materials composed of inorganic metal centers and organic ligands, MOFs enable the targeted design of magnetic behavior [2] and facilitate the integration of magnetism with additional physical functionalities such as conductivity [3], frustration [4], or adsorption [5].

A first reference point for this strategy is **$Cu(ta)_2$**, composed of condensed Kuratowski units exhibiting a characteristic Jahn-Teller distortion [6]. Magnetic studies revealed partial spin frustration among the copper centers [6]. This raised the question of how structural variations could modulate such magnetic behavior. Inspired by this, structurally related Kuratowski-type complexes with reduced interunit interactions were synthesized, showing weak antiferromagnetic exchange [7].

Extending this concept to other metal ions highlighted the versatility of the H-ta ligand. $[Fe(ta)_2]$ displayed the largest reported thermal hysteresis for a cooperative spin crossover (SCO) at elevated temperatures [8], while the centred pyrochlore lattice of $[Mn(ta)_2]$ exhibited pronounced magnetic frustration, consistent with Coulomb phase behaviour of a classical spin liquid [9]. Replacing the metal with chromium shifted the magnetic ground state to ferromagnetic, yielding a Curie temperature of 225 K and strong negative magnetoresistance at 5 K [10].

To directly probe the effect of steric control, organic substituents were introduced at the H-ta linker. In the case of $[Fe(ta)_2]$, even subtle steric modifications led to a downshift in the SCO temperature, confirming the sensitivity of this phenomenon to small structural changes [11]. Continuing this line of research, the present study reveals the locking of local coordination geometry in **$Cu(ta)_2$** derivatives. While 4,5-dimethyl-1H-1,2,3-triazole (H-dmta) did not form Kuratowski-type units [4,12]-methyl-1*H*-1,2,3-triazole (H-mta) and 1,4,5,

☆ During the preparation of this work the authors used deeplwrite in order to spellcheck. After using this tool, the authors reviewed and edited the content as needed and take full responsibility for the content of the publication.

* Corresponding author.
E-mail address: dirk.volkmer@physik.uni-augsburg.de (D. Volkmer).

https://doi.org/10.1016/j.jpcs.2026.113566
Received 17 October 2025; Received in revised form 26 January 2026; Accepted 27 January 2026
Available online 28 January 2026

6-Tetrahydrocyclopenta-1*H*-1,2,3-triazole (H-cta) yielded more rigid, condensed frameworks with reduced pore volume, structures in which the Jahn–Teller effect can be tuned such that the static Jahn-Teller distortion can be shifted by keeping the neighbouring atoms of copper in place.

The Jahn-Teller effect, a key factor in structural distortions of transition-metal complexes, arises from electronic degeneracy and can be alleviated through elongation or compression of the metal–ligand bonds [13]. Controlling this distortion not only stabilizes the system but also directly shapes its electronic, magnetic, and optical properties [14], making steric tuning of triazole ligands a powerful approach for designing MOFs with targeted functionalities.

Therefore, preparation procedures for the novel **Cu(mta)$_2$** (H-mta = 4-methyl-1*H*-1,2,3-triazole) and **Cu(cta)$_2$** (H-cta = 1,4,5,6-Tetrahydrocyclopenta-1*H*-1,2,3-triazole) metal-organic frameworks, which feature the same condensed Kuratowski units as **Cu(ta)$_2$**, were optimized. The resulting MOF structures were characterized by single-crystal X-ray diffraction (SC-XRD), powder X-ray diffraction (PXRD), variable-temperature PXRD (VT-PXRD), thermogravimetric analysis (TGA), argon adsorption, and attenuated total reflectance Fourier transform infrared spectroscopy (ATR-FT-IR). To deepen the understanding of the magnetic properties of the framework, electron spin resonance (ESR) as well as magnetic susceptibility and magnetization measurements in conjunction with simulations were applied.

2. Experimental section

Materials

N,*N*-dimethylformamide (99.8 % analytical grade; VWR), ethanol (99.8 % analytical grade; VWR), methanol (99.8 % analytical grade; VWR), ammonia solution (25 % technical grade, VWR), copper(II)hydroxide (technical grade; Sigma-Aldrich), copper(II)sulfate pentahydrate (99.999 %; Sigma-Aldrich) were used as received from the commercial supplier.

Syntheses

1,4,5,6-Tetrahydrocyclopenta-1*H*-1,2,3-triazole (H-cta) was prepared according to the literature procedure [15] and purified further via sublimation. Methyl-1H-1,2,3-triazole (H-mta) was prepared according to the literature procedure [11].

Cu(ta)$_2$ was prepared according to literature [6].

Synthesis of Cu(mta)$_2$

$Cu(OH)_2$ (150 mg, 1.54 mmol) was dissolved in NH_4OH (20 mL, 25 %) and **H-mta** (258 mg, 0.312 mmol) dissolved in EtOH (20 ml) was added. The resulting turquoise suspension was placed in a DURAN® culture tube, sealed with a Teflon lined screw cap and heated in a heating block at 120 °C for 3 d. The product was centrifuged and washed 3 times with 50 mL of a H_2O/EtOH (1:1) mixture. Drying for 4 h under vacuum at RT afforded the phase pure product as a turquoise powder (240 mg, 68 %).

FT-IR (ATR) 4000–180 cm^{-1}: 3129 (w), 2927 (m), 1657 (w), 1547 (m), 1531 (m), 1455 (w), 1390 (m), 1371 (m), 1307 (m), 1231 (m), 1216 (m), 1193 (m), 1169 (m), 1114 (s), 1089 (m), 1055 (m), 1019 (s), 830 (s), 713 (w), 680 (w), 671 (s) (Fig. S1).

Synthesis of Cu(mta)$_2$ single crystals

H-mta (25.8 mg, 0.310 mmol) was dissolved in a mixture of NH_4OH (2 mL, 25 %) and EtOH (2 mL) in a DURAN® culture tube and the Cu $(OH)_2$ (15 mg, 0.154 mmol) was placed ca. 8 cm above the solvent level in a folded 25 mm filtration paper circle. The tube was sealed with a Teflon lined screw cap and heated in a heating block at 120 °C for 3 d resulting in turquoise single crystals and smaller particles.

Synthesis of Cu(cta)$_2$

$CuSO_4{\cdot}5H_2O$ (38.4 mg, 0.154 mmol) was dissolved in NH_4OH (2 mL, 25 %) and **H-cta** (33.8 mg, 0.310 mmol) dissolved in EtOH (2 mL) was added. The resulting turquoise suspension was placed in a DURAN® culture tube, sealed with a Teflon lined screw cap and heated in a heating block at 120 °C for 2 d. The product was centrifuged and washed 3 times with 5 mL of a H_2O/EtOH (1:1) mixture. Drying for 4 h under vacuum at RT afforded the phase pure product as a turquoise powder (33 mg, 77 %). FT-IR (ATR) 4000–180 cm^{-1}: 2975 (m), 2923 (m), 2856 (m), 1531 (m), 1500 (w), 1439 (w), 1266 (w), 1213 (m), 1176 (m), 1144 (w), 1077 (s), 1023 (m), 901 (m), 837 (w), 727 (m), 675 (w), 576 (s); elemental analysis calcd (%) for $C_{10}H_{12}N_6Cu$: C 42.93H 4.32 N 30.04; found: C 42.59H 4.53 N 29.74. (Fig. S2).

Synthesis of Cu(cta)$_2$ single crystals

H-cta (33.8 mg, 0.310 mmol) was dissolved in a mixture of NH_4OH (2 mL, 25 %) and EtOH (2 mL) in a DURAN® culture tube and the Cu $(OH)_2$ (15 mg, 0.154 mmol) was placed ca. 3 cm above the solvent level in a folded 25 mm filtration paper circle. The tube was sealed with a Teflon lined screw cap and heated in a heating block at 120 °C for 1 d resulting in large green/turquoise single crystals and smaller particles. SEM micrographs comparing Bulk with single crystal synthesis are shown in Fig. S3.

Attenuated total reflectance (ATR) infrared spectroscopy. Fourier transform infrared (FT-IR) spectra were recorded in the range of 4000–400 cm^{-1} with a Bruker Equinox 55 FT-IR spectrometer equipped with the PLATINUM ATR unit and a KBr beam splitter. The signals were labelled as strong (s), medium (m), weak (w), and broad (br).

Thermogravimetric analysis. A TA Instruments Q500 thermogravimetric analyser was used to obtain the thermogravimetric analysis (TGA) data, which was recorded after a 5 min isothermal step in the temperature range of 25–700 °C with a heating rate of 10 K min^{-1} under a nitrogen gas stream.

Scanning electron microscopy (SEM). SEM micrographs were recorded on a Zeiss Crossbeam 550 scanning electron microscope and a Zeiss Merlin 450.

Powder X-Ray diffraction (PXRD). The PXRD and VT-PXRD patterns were collected with a Malvern Panalytical Empyrean diffractometer equipped with a Bragg-Brentano^{HD} mirror, a PIXcel^{3D} 2 × 2 detector, and a XRK 900 reactor chamber with 0.026° steps and a measurement time of 1595 s for each pattern in the range of 3–50° 2θ. The samples were heated with 25 °C steps up to 300 °C and in 50 °C steps up to 500 °C with a 5 °C/min heating rate under nitrogen atmosphere.

Single-crystal X-ray diffraction and structure refinement. Single-crystal X-ray diffraction data set was collected with a Bruker D8 Venture diffractometer equipped with a low-temperature device at room temperature. APEX4 (v2021.10–0) software [16] was used for collecting, initial indexing and processing of the intensities. The raw data frames were integrated and corrected for absorption effects using the Bruker SAINT [17] and SADABS [18] software packages. The structures were solved and refined using the Bruker SHELXTL Software Package [19]. All non-hydrogen atoms were refined anisotropically. It was not possible to refine the solvent molecules in the voids; hence, the SQUEEZE [20] procedure was applied to the data. Selected crystal data and the refinement details are listed in Table 1. Complete crystallographic data for the structures reported in this paper can be obtained from the Cambridge Crystallographic Data Centre as supplementary publication No. (2488278 and 2488279).

Magnetic measurements

ESR measurements were performed in a continuous wave

Table 1
Crystal data and structure refinement for **Cu(mta)$_2$ and Cu(cta)$_2$**.

Empirical formula	$C_6H_8CuN_6$	$C_{10}H_{12}CuN_6$
Formula weight [gmol^{-1}]	227.72	279.80
Temperature [K]	301(2)	297(2)
Crystal system	tetragonal	Cubic
Space group	$P4_12_12$	Fd-3m
Unit cell dimensions a [Å]	11.7671(2)	18.0758(2)
Unit cell dimensions b [Å]	11.7671(2)	18.0758(2)
Unit cell dimensions c [Å]	19.1161(4)	18.0758(2)
α[°]	90	90
β[°]	90	90
γ[°]	90	90
Volume/Å^3	2646.90(11)	5906.0(2)
Z	12	24
Density (calculated) [gcm^{-3}]	1.714	1.888
Absorption coefficient [mm^{-1}]	2.435	2.203
F(000)	1380.0	3432.0
2Θ range for data collection [°]	4.896 to 54.974	6.376 to 54.802
Index ranges	$-12 \leq h \leq 15$, $-15 \leq k \leq 15$, $-24 \leq l \leq 24$	$-23 \leq h \leq 23$, $-23 \leq k \leq 23$, $-23 \leq l \leq 23$
Reflections collected	40790	32596
Independent reflections	3039 [$R_{int} = 0.1059$, $R_{sigma} = 0.0379$]	366 [$R_{int} = 0.0399$, $R_{sigma} = 0.0061$]
Data/restraints/parameters	3039/192/258	366/4/41
Goodness-of-fit on F^2	1.140	1.071
Final R indexes [I ≥ 2σ (I)]	$R_1 = 0.0655$, $wR_2 = 0.1338$	$R_1 = 0.0449$, $wR_2 = 0.1064$
Final R indexes [all data]	$R_1 = 0.0732$, $wR_2 = 0.1377$	$R_1 = 0.0474$, $wR_2 = 0.1082$
Largest diff. peak/hole [e Å^{-3}]	0.95/-1.01	0.46/-0.70

spectrometer (Bruker ELEXSYS E500A) working at X-band frequency in the temperature region $4 \leq T \leq 300$ K using a continuous He gas-flow cryostat (Oxford Instruments) (microwave frequency $\nu = 9.45$ GHz). For the measurement from $300 \leq T \leq 450$ K a Nitrogen gas-flow cryostat (Bruker) ($\nu = 9.47$ GHz) was used. The measurement was done with a power of 20 mW, a gain of 60 dB, a login field modulation of 100 kHz, a modulation amplitude of 10 G and a conversion time of 60 ms. The temperature stabilized hall-probe was calibrated using a DPPH sample.

Magnetic susceptibility and magnetization measurements were performed using a superconducting quantum interference device (SQUID) magnetometer (Quantum Design, MPMS5) working in the temperature range of $1.8 \leq T \leq 400$ K in magnetic fields up to 5 T.

3. Results and discussion

3.1. Characterization

The PXRD patterns of the bulk **Cu(cta)$_2$** and **Cu(mta)$_2$** show a good match with the patterns calculated from the single-crystal structure determination (Fig. S4), thus, verifying the phase purity of the material. The thermal stability of **Cu(mta)$_2$** and **Cu(cta)$_2$** was investigated with VT-PXRD (Fig. S5) measurements, showing a decrease of crystallinity at 533 K and 493 K and a complete loss of crystallinity at 593 K or 523 K respectively, which coincides well with the first large weight loss step starting at 260 °C and 200 °C in the TGA curve (Fig. S6).

3.2. Structural description

3.2.1. Cu(ta)$_2$

Cu(ta)$_2$ has two phases, a cubic high temperature phase (beta phase) (Fd $\bar{3}$ m (227)) and a tetragonal space/low temperature phase (alpha phase) ($I4_1$/amd (141)) [6]. Both have 2 different copper sites in a ratio of 2 to 1. The most important distances between the low and high temperature phases are shown in Table 2. Distortion to the low-temperature phase takes place at copper site 2 where the octahedron is elongated (Jahn-Teller distortion).

3.2.2. Cu(mta)$_2$ and Cu(cta)$_2$

Single crystal X-ray structural analysis reveals that **Cu(mta)$_2$** crystallizes in the tetragonal crystal system in the space group $P4_12_12$ (no. 92), whereas **Cu(cta)$_2$** crystallizes in the cubic phase (Fd $\bar{3}$ m (227)). The asymmetric unit of **Cu(mta)$_2$** contains two copper, 12 nitrogen, 12 carbon and 12 hydrogen atoms, while the **Cu(cta)$_2$** contains two copper, 2 nitrogen, 3 carbon and 3 hydrogen atoms. Both asymmetric units are shown in Fig. S7.

Cu(mta)$_2$ shows some disorder in the methyl-group of its linker. C1A-C3A and C10A-C12A are disordered around a 2-fold rotation axis with direction [1, −1, 0] at x, -x, ¼ and have therefore a 50 % probability. Other have a disorder of C5A-C7A 54 % and C5B–C7B 46 %, CB4, C8B and C9B 20 % and CA4, C8A and C9A 80 %. The Hydrogen atoms have the same probability as the respective Carbon atoms.

Cu(cta)$_2$ shows some disorder in the top part of its linker. Their probability is C3 50 %, with their respective Hydrogen having the same probability.

The disorder of the MTA units could be the reason for the lower symmetry space group compared to **Cu(cta)$_2$** and **Cu(ta)$_2$**. ORTEP style plots of the asymmetric units for both MOFs are shown in Fig. 1.

As shown in Fig. 2, **Cu(mta)$_2$** and **Cu(cta)$_2$** comprise coordination units, in which the Cu(II) metal ions are coordinated by six tridentate methyl-triazolate ligands via nitrogen donor atoms. In **Cu(mta)$_2$** the d^9 Cu(II) ions are placed in CuN_6 octahedra which show two different kinds of distortion. The Cu1 centers has 4 different bond distances, two times 2.399 and 2.04 opposing each other in the same plane and out of this plane the two other distances are 2.13 and 2.043. The Cu2 centers is distorted in all directions. In **Cu(cta)$_2$** there are also two different Cu sites, but both show no distortion in the Sc-crystal measurement, with distances to nitrogen from Cu1 2.177 and from nitrogen's to Cu2 2.133. Both compounds contain Kuratowski-type SBUs.

Within each SBU four Cu(II) ions occupy the vertices of an imaginary tetrahedron and the central Cu2 atom is coordinated to six triazolate based ligands. In the case of **Cu(cta)$_2$**, a perfect tetrahedron can be seen (Cu1 atoms are placed at equal distances of 6.3908 Å), whereas a distorted tetrahedron is observed in **Cu(mta)$_2$** (non-bonding Cu–Cu distances of 6.392 and 5.889 Å, respectively) see Table 3.

The atomic coordinates, isotropic thermal parameters, selected bond lengths and angles for **Cu(mta}$_2$** are given in Tables S1–S7 and for **Cu (cta)$_2$** in Tables S8–S14.

3.3. Magnetic properties

The magnetic properties of the 3 MOFs were analyzed using SQUID and ESR data. For clarity, all 3 MOFs are described individually with

Table 2
Overview of the bond distances in low and high temperature phase of Cu(ta)$_2$ [6].

	Cu(ta)$_2$ alpha	Cu(ta)$_2$ beta
Temperature (K)	295	473
Cu1 Cu1 (Å)	5.9223	6.167
Cu2 Cu2 (Å)	7.5885	7.552
Cu1 Cu2 (Å)	3.7942	3.776
Cu1 N1 (Å)	2.186	2.175
Cu2 N2 (Å)	2.040 (4 times)	2.316 (6 times)
Cu2 N4 (Å)	2.348 (2 times)	

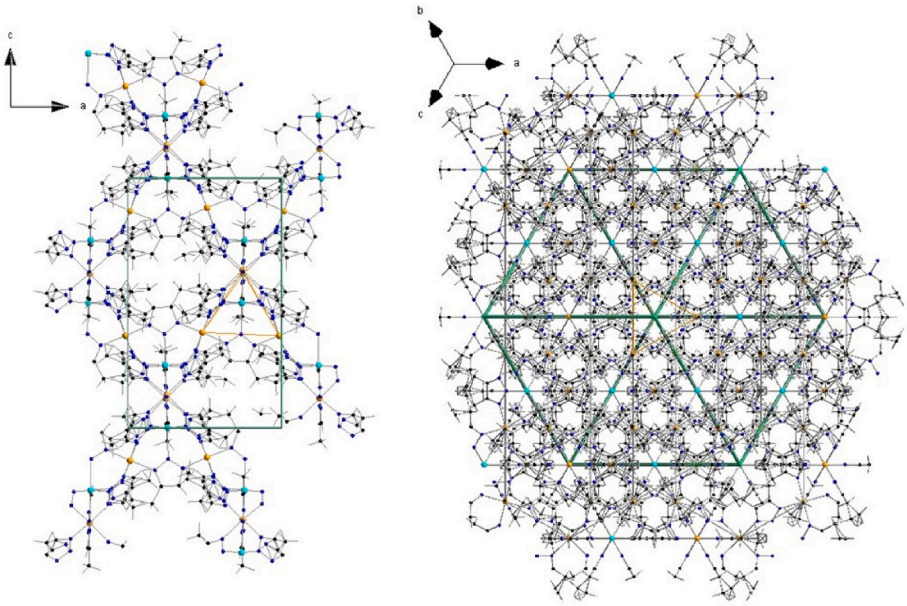

Fig. 1. Packing of **Cu(mta)$_2$** (left) and **Cu(cta)$_2$** (right) drawn in the ball-stick style. For clarity, all disordered atoms except those caused by symmetry have been omitted. In green lines are the unit cell edges, the yellow lines in the middle outline the respective tetrahedrons which are shown enlarged in Fig. 2. (For interpretation of the references to colour in this figure legend, the reader is referred to the Web version of this article.)

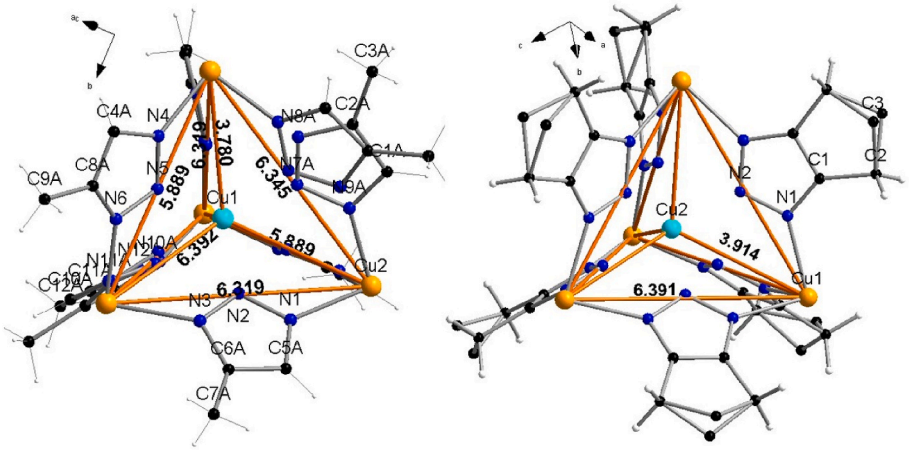

Fig. 2. Non-bonding Cu–Cu distances represented by imaginary tetrahedra (orange lines) in of **Cu(mta)$_2$** (left) and **Cu(cta)$_2$** (right) drawn in the ball-stick style. (For interpretation of the references to colour in this figure legend, the reader is referred to the Web version of this article.)

Table 3
Selected atom distances in **Cu(mta)$_2$** and **Cu(cta)$_2$**.

	Cu(mta)$_2$	Cu(cta)$_2$
Temperature (K)	295	295
Cu1 Cu1 (Å)	7.582	6.3908
Cu2 Cu2 (Å)	5.889 & 5.889	7.8271
Cu1 Cu2 (Å)	3.78	3.9135
Cu1 N (Å)	2.399 (2 times), 2.04 (2 times), 2.13, 2.043	2.177 (6 times
Cu2 N (Å)	2.02, 2.206, 2.004, 2.0025, 2.132, 1.963	2.133 (6 times)

their respective measurements and are compared at the end. The order is according to the size of the linkers.

3.3.1. *Cu(ta)$_2$*

Magnetic susceptibility measurements of the polycrystalline **Cu(ta)$_2$** sample were performed in a magnetic field of 10000 Oe for temperatures between 1.8 and 400 K. The temperature dependence of the molar susceptibility $\chi_m(T)$, the product $\chi_m T$ (T), and the inverse molar susceptibility $\chi_m^{-1}(T)$ is shown in Fig. 3. Starting from high temperature, the susceptibility $\chi_m(T)$ increases gradually on decreasing temperature and diverges at low temperatures. The $\chi_m^{-1}(T)$ behavior can be divided into two different regimes. In the high temperature regime, above 100 K, it follows a Curie-Weiss law with a Curie constant C_{hT}=0.42 emu mol^{-1} K. This is 12 % above the spin only value for 1 uncoupled spin ½ per formula unit (C_{theo} = 0.375 emu mol^{-1} K assuming g = 2). The resulting g = 2.14 is typical for Cu^{2+} ions in octahedral ligand field with nearly quenched orbital contributions [21]. The Curie-Weiss temperature θ_{CW} = −45 K indicates an antiferromagnetic behavior. In the low temperature regime, below 50 K, the inverse susceptibility drops faster but keeps the antiferromagnetic behavior. The product $\chi_m T$ (T) declines steadily with decreasing temperature until it drops faster below 150 K towards 0.075 at 1.8K, the lowest accessible temperature in our magnetometer. Toward room temperature $\chi_m T$ (300 K) = 0.38 emu K/mol reaches approximately the value expected for 1 free spin per formula unit in the

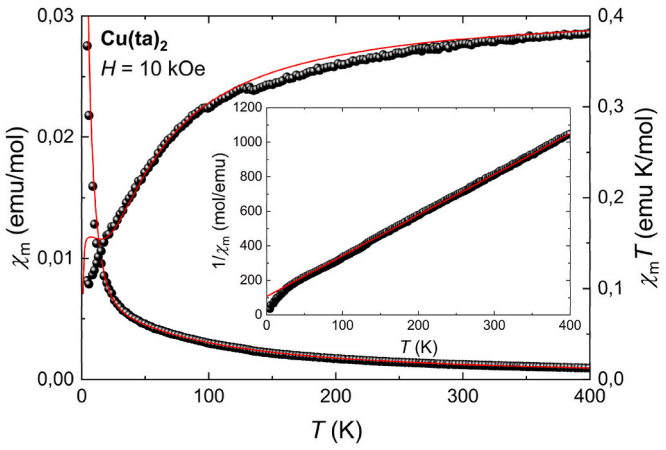

Fig. 3. Temperature dependence of the molar susceptibility χ_m(T) and product χ_mT(T) at 10000 Oe. Open symbols show the experimental data. Red solid lines represent fit 1 based on the Hamiltonian $\widehat{H}_1$ given in the text. Inset: Inverse molar susceptibilities $1/\chi_m$(T) fitted with 1 Ci Weiss law. (For interpretation of the references to colour in this figure legend, the reader is referred to the Web version of this article.)

high temperature limit (resembling the Curie constant). At around 10 K the value of $\chi_m T$ (10 K) = 0.12 emu K/mol corresponds to 1/3 spin per formula unit (0.125 emu K/mol g = 2), i.e. 1 spin per 3 copper ions on a simplified triangular structural motif with antiferromagnetic exchange interactions as will be detailed below.

Magnetization curves $M(H)$ of the sample were measured in magnetic fields H up to 5 T at temperatures of 2, 5, and 10 K as shown in Fig. 4. The asymptotic saturation value of the magnetization at 10 K and lower, determined with a Brillouin function again shows only 1/3 of the expected value for a Cu^{2+} spin per formula unit in agreement with the low-temperature susceptibility data, i.e. two spins out of three compensate each other due to antiferromagnetic interactions between the spins.

To gain a deeper understanding the magnetic behavior was analyzed using the program PHI [22] to model the molar susceptibility and magnetization data with a molecular approach for exchange-coupled Cu (II) ions. In general, the exchange interactions and g-factors must be treated as tensors, and their spatial orientation must be considered in the

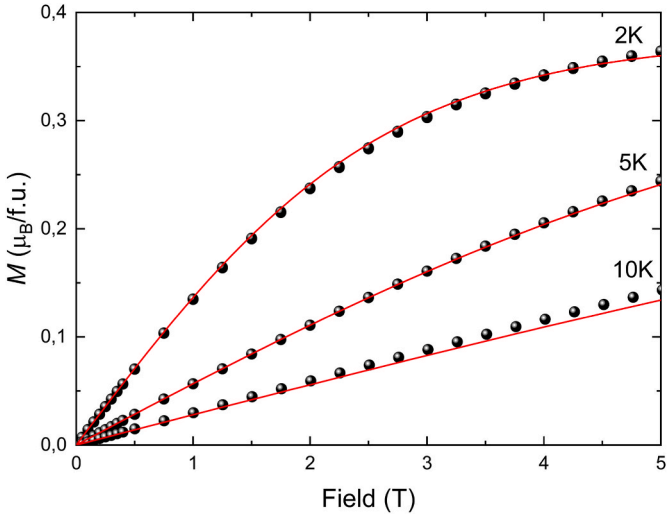

Fig. 4. Field-dependent magnetization curves M(H) at 2, 5 and 10 K. Open symbols show the experimental data, red solid lines represent fit 1 based on the Hamiltonian $\widehat{H}_1$ given in the text. (For interpretation of the references to colour in this figure legend, the reader is referred to the Web version of this article.)

calculation. However, as measurements were done on polycrystalline material, the anisotropies are averaged out. Note that the anisotropic contribution to the exchange interaction is of the order of $\left(\frac{\Delta g}{g}\right)^2$ where Δg denotes the anisotropy of the g-tensor, which amounts about 0.3 for Cu^{2+} in octahedral ligand field. With an average g-factor of g = 2.2, typical for Cu^{2+}, we obtain an anisotropic exchange less than 2 %. Consequently isotropic exchange is dominant and anisotropic contributions are within the error bar [23]. Therefore, the fit parameters could be reduced to the following isotropic Heisenberg–Dirac–van Vleck (HDVV) spin Hamiltonian for the exchange coupling combined with terms for the Zeeman splitting in the external magnetic field $\vec{H}$. In the formula below, the following notation is used: exchange coupling J as shown in Fig. 5, spin S, g-factor g and μ_B Bohr magneton.

$$\widehat{H}_1 = -2J_1\,\vec{S}_1\vec{S}_2 - 2J_1\,\vec{S}_1\vec{S}_3 - 2J_2\,\vec{S}_2\vec{S}_3 + g_1{}^*\mu_B\vec{S}_1{}^*\vec{H} + g_2{}^*\mu_B\vec{S}_2{}^*\vec{H} + g_3{}^*\mu_B\vec{S}_3{}^*\vec{H} \quad (1)$$

This simplified model reduces the MOF structure to triangles of exchange-coupled spins which reflect the basic interactions between the magnetic ions in the present compounds under consideration. The above Hamiltonian gives reasonable estimations of the exchange interactions and simultaneously fits with the temperature-dependent susceptibility and the field-dependent magnetization data using the parameters $J_1/k_B = -23.8(5)$ K, $J_2/k_B = -36.8(5)$ K, $g_1 = 2.26$, $g_2 = g_3 = 2.01$. This means that the g-factor of the central Cu^{2+} spin S_1 in a stretched octahedral environment is significantly higher at $g_1 = 2.26$, while for the peripheral Cu^{2+} spins S_2 and S_3 in a compressed octahedral environment it is very close to the value of the free electron at $g_2 = 2.01$. The resulting average g-factor of g = 2.09 is still in good agreement with the value of g = 2.14 determined from the Curie-Weiss law, since the Curie-Weiss estimate was done without any corrections concerning diamagnetic and van-Vleck contributions. Moreover, because of the uncertainty of the mass, due to the porosity of the MOFs, one generally may overestimate the mass and hence underestimate the g-value when evaluating the SQUID susceptibility data which depend on the product of the number of spins and squared g-factor. Thus, in case of $Cu(ta)_2$, the modeling with the program PHI, which takes into account a temperature independent susceptibility contribution, yields a slightly smaller g factor due to the uncertainty in mass. The stronger antiferromagnetic coupling J_2 results in an effective compensation of the spins S_2 and S_3 at low temperatures and hence explains the observed saturation plateau at 1/3 of the full saturation magnetization due to the remaining spin S_1.

To investigate the magnetic properties in more detail, powder ESR measurements were performed at X-band frequency (9.48 GHz) at temperatures from 5 to 450 K on a Bruker Elexsys II CW spectrometer (different cryostats). The ESR spectra at 5 K, 50 K, 100 K and 200 K are illustrated in Fig. 6. The data shown is fitted using an uni-axial powder pattern, i.e. the sum of Lorentzian lines geometrically weighted over all possible orientations of the uniaxial g tensors of the powder grains from parallel (g‖‖) to perpendicular (g⊥) to the external magnetic field. Note that due to the strong exchange interaction the g-tensor represents the symmetry of the exchange-coupled Cu(1)–Cu(2) triangular complex, i.e. the contributions of the different copper sites cannot be resolved. The intensity had to be calculated by two-fold numerical integration of the spectra. This "double-integrated intensity" I_{ESR} is equivalent to the pure spin susceptibility without any diamagnetic and van-Vleck contributions. This is illustrated by the fact that the inverse intensity $1/I_{ESR}(T)$ determined from the ESR measurements is consistent with the susceptibility from SQUID data, as seen in Fig. 6. Here, the scaling factor depends on the measurement settings and only the proportionality was checked. The fitting of the ESR data was performed with a fit program developed at our institute in Augsburg: Spectrolyst. Fitting the intensity with the plot program ORIGIN using a Curie -Weiss-law leads to Curie-

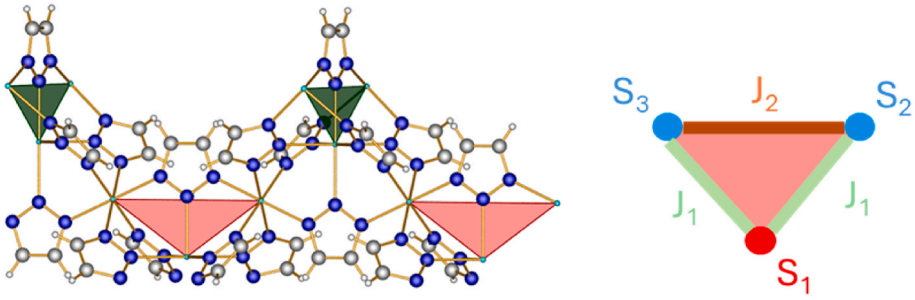

Fig. 5. Representation of **Cu(ta)$_2$** MOF as an alternating triangular system and the basis for the model.

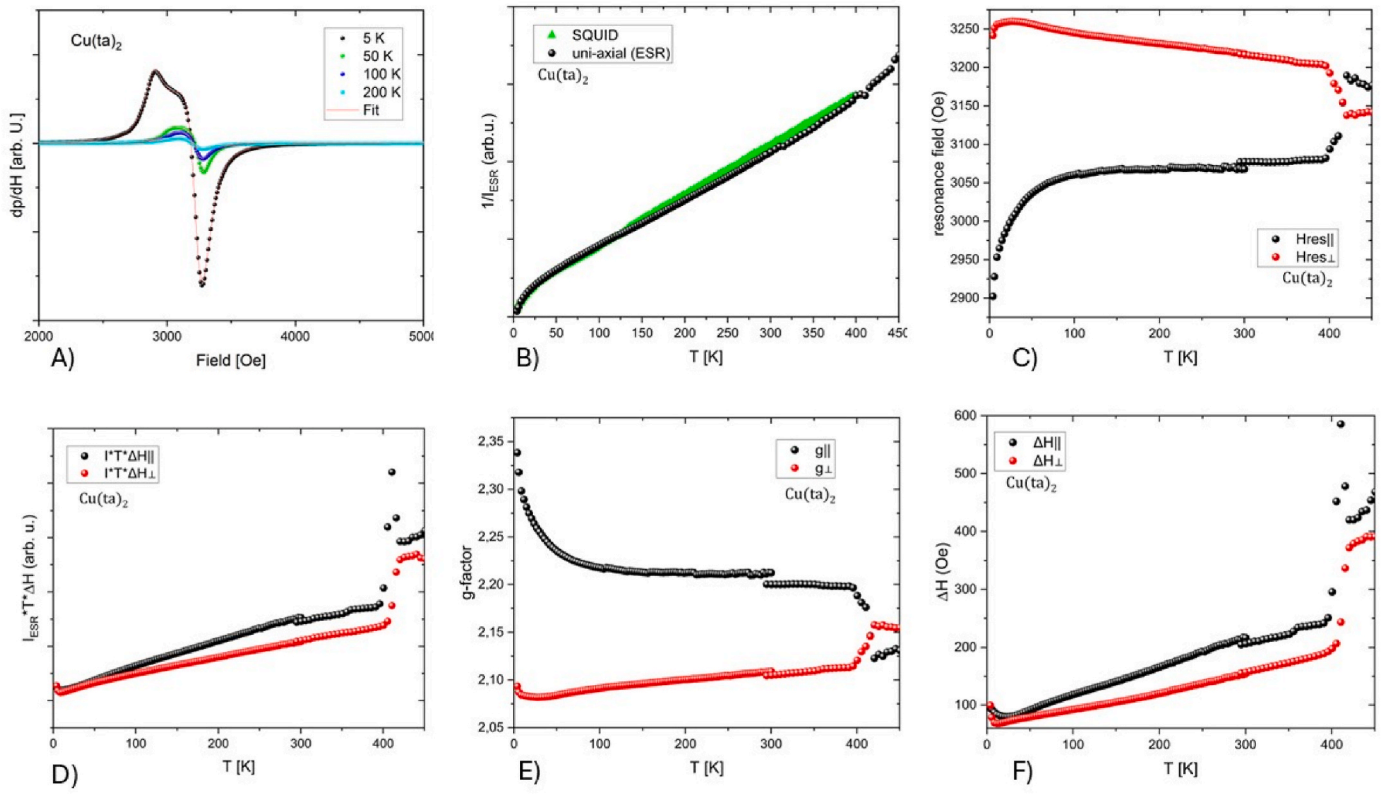

Fig. 6. A) ESR spectra (X-band, 9.48 GHz) of **Cu(ta)$_2$**, closed symbols show the experimental data at 5 K red solid lines represent the uni-axial fit. B) Inverse ESR intensities plotted against temperature compared with the inverse molar susceptibility $1/\chi$m(T). C) Resonance field plotted against temperature. D) the product I_{ESR}•**T**•ΔH is plotted against temperature. E) Temperature dependence of the g-factor. F) Linewidth ΔH plotted against temperature. (For interpretation of the references to colour in this figure legend, the reader is referred to the Web version of this article.)

Weiss temperatures of $\theta_{CW} = -72$ K. The discrepancy with respect to the Curie–Weiss temperature obtained from the Curie-Weiss fit of the SQUID susceptibility can be attributed to the fact that diamagnetic corrections were not taken into account in that analysis. Such corrections have no influence on ESR measurements; therefore, the Curie–Weiss temperatures derived from ESR are considered to be more reliable. At room temperature, *g*-factors of $g_{||} = 2.22$ and $g^{\perp} = 2.12$ are observed, which agrees reasonably with the findings of the SQUID measurements. A slight influence of the temperature dependence towards lower temperatures on the g-factors can be observed shifting the higher up to 2.34 and pushing the lower to 2.10. These shifts can be explained by the increasing local fields originating from the temperature dependence of the magnetic susceptibility as well as by the fact that at low temperatures the stronger g-anisotropy of S_1 effectively dominates. The jump at 300 K is due to the cryostat switch, and the abrupt change at 400 K is due to a Jahn-Teller transition, which can also be seen in the DSC measurements [6].

The linewidth is determined by the half width at half maximum (HWHM) of the Lorentzian fit. Both directions exhibit a similar trend in their line width, demonstrating a decrease from low temperatures, a minimum at 10–20K, and subsequently an increase towards higher temperatures. The increase to higher temperatures can be explained on the basis of electron-phonon interaction [24]. In general, if the main contribution to the linewidth is the spin-spin interaction in an insulator, a plot of $\Delta H^*T^*\chi_a(0)$ versus temperature would approach a constant value at high temperature. If the product continues to increase with temperature, the spin-phonon relaxation is not negligible [24]. The substitution of $\chi_a(0)$ with I_{ESR} is valid since the magnetic susceptibility and the ESR intensities behave the same. At 400 K a sharp increase of the linewidth can be seen which is due to a Jahn-Teller transition. It is behaving like a first order transition; therefore, the transition could not be fit in terms of an Arrhenius law, which would allow to extract the excitation energy.

3.3.2. $Cu(mta)_2$

Magnetic susceptibility measurements of the polycrystalline **Cu(mta)$_2$** sample were performed in a magnetic field of 10000 Oe for temperatures between 1.8 and 300 K. The temperature dependence of the molar susceptibility χ_m(T), the product χ_mT (T), and the inverse molar susceptibility χ_m^{-1}(T) is shown in Fig. 7. It exhibits a very similar behavior like **Cu(ta)$_2$** as it follows a Curie-Weiss law with a Curie constant C_{hT}=0.403 emu mol^{-1} K. This is about 7 % above the spin only value for 1 free spin ½ per formula unit. The resulting g = 2.07 is still in the range for Cu^{2+} ions in octahedral ligand field with nearly quenched orbital contributions [21]. The Curie-Weiss temperature θ_{CW} = −50 K indicates an antiferromagnetic behaviour. Around room temperature $\chi_m T$ (300 K) = 0,36 emu K/mol is close to the value expected for 1 free spin S = ½ per formula unit. At around 10 K $\chi_m T$ (10 K) = 0.15 emu K/mol corresponds to 1/3 uncoupled S = ½ spins per formula unit, which fits to 1 copper ion per triangle.

Magnetization curves *M*(*H*) of the sample were measured in magnetic fields *H* up to 5 T at temperatures of 2 and 10 K as shown in Fig. 8. The asymptotic saturation value of the magnetization at 10 K and lower, determined with a Brillouin function, shows again only 1/3 of the expected value for a Cu^{2+} spin due to the antiferromagnetic interactions between the spins.

For further analysis the magnetic behavior was modelled with the same approach as **Cu(ta)$_2$** (see Fig. S8) using the program PHI [22]. Leading to J_1/k_B = −15.8(5) K, J_2/k_B = −38.8(5) K, g_1 = 2.27, $g_2 = g_3$ = 2.0. This means that the central Cu^{2+} spin S_1 and the peripheral Cu^{2+} spins S_2 and S_3 show the same behavior as in **Cu(ta)$_2$**. The resulting average g-factor of g = 2.09 is slightly higher than the g-factor determined by the Curie-Weiss law. The strong antiferromagnetic J_2 value again explains the residual saturation at 1 μ_B per triangle by vice versa compensation of S_2 and S_3.

To focus on the local magnetic properties in more detail, powder ESR measurements were performed up to 300 K on the same device as for the **Cu(ta)$_2$** and towards 450 K on the nitrogen gas flow cryostat. The slight shift at 300 K in the data is due to the device switch.

The ESR spectra at 5 K, 50 K, 100 K and 200 K are illustrated in Fig. 9. The data shown is fitted using an uni-axial powder pattern as mentioned above. As for **Cu(ta)$_2$** the inverse intensity is in good agreement with the susceptibility from SQUID measurement as seen in Fig. 9. The fitting of the ESR data leads to a Curie-Weiss temperature of θ_{CW} = −52 K. At

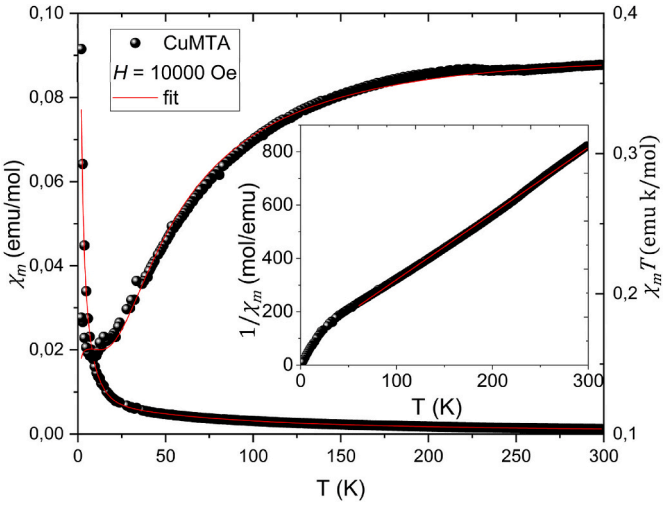

Fig. 7. Temperature dependence of the molar susceptibility χ_m(T) and product χ_mT(T) at 10000 Oe. Open symbols show the experimental data. Red solid lines represent fit 1 based on the Hamiltonian $\hat{H}_1$ given in the text. Inset: Inverse molar susceptibilities $1/\chi_m$(T) fitted with 1 Ci Weiss law. (For interpretation of the references to colour in this figure legend, the reader is referred to the Web version of this article.)

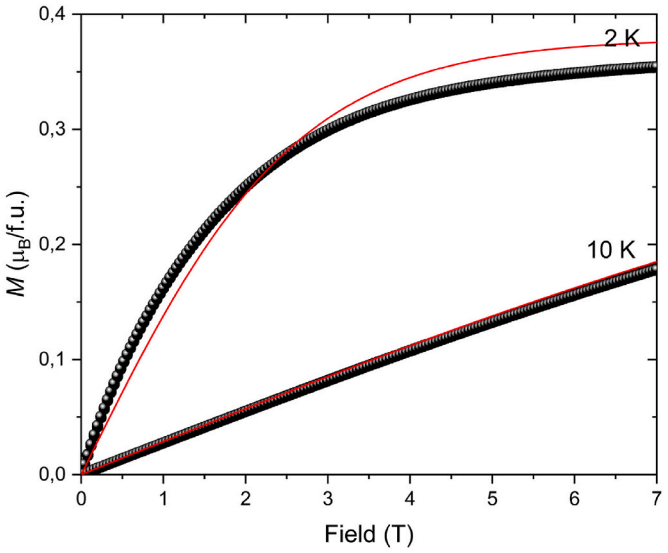

Fig. 8. Field-dependent magnetization curves M(H) at 2, 5 and 10 K. Open symbols show the experimental data, red solid lines represent fit 1 based on the Hamiltonian $\hat{H}_1$ given in the text. (For interpretation of the references to colour in this figure legend, the reader is referred to the Web version of this article.)

room temperature *g*-factors of $g_{||}$ = 2.2(2) and $g^{\perp}$ = 2.1(2) are observed, which agrees with the findings of the SQUID measurements. A slight influence of the temperature on the g-factors can be observed shifting the higher up to 2.34(2) and pushing the lower to 2.08(2) on cooling to 1.8 K. Like in the previous case this is due to the local antiferromagnetic alignment of the copper spins and the stronger anisotropy of the residual spin. The linewidth is determined by the half width at half maximum (HWHM) of the Lorentzian fit. Both directions exhibit a similar trend in their line width, demonstrating a decrease from low temperatures, a minimum at 100 K, and subsequently an increase towards higher temperatures. Like for **Cu(ta)$_2$** the increase at higher temperatures can be explained on the basis of electron-phonon interaction [24]. But note that there is no sudden increase at high temperatures, i.e. no transition into the dynamical Jahn-Teller regime up to 450 K.

3.3.3. $Cu(cta)_2$

Magnetic susceptibility measurements of the polycrystalline **Cu(cta)$_2$** sample were performed in a magnetic field of 10000 Oe for temperatures between 1.8 and 300 K. The temperature dependence of the molar susceptibility χ_m(T), the product χ_mT (T), and the inverse molar susceptibility χ_m^{-1}(T) is displayed in Fig. 10. It shows again a similar behavior like **Cu(ta)$_2$** as it follows a Curie-Weiss law with a Curie constant C_{hT}=0.41 emu mol^{-1} K. This is about 9 % enhanced with respect to the spin only value for 1 uncoupled spin ½. The resulting g = 2.09 is also in the range for Cu^{2+} ions in octahedral ligand field with nearly quenched orbital contributions [21]. The Curie temperature θ_{CW} = −24 K again indicates an antiferromagnetic behavior. Around room temperature $\chi_m T$ (300 K) = 0.37 emu K/mol is close to the value expected for 1 uncoupled S = ½ spin per formula unit. Approaching zero temperature $\chi_m T$ (10 K) = 0.15 emu K/mol corresponds once more to 1/3 uncoupled S = ½ spins, i.e. 1 copper spin per triangle.

Magnetization curves *M*(*H*) of the sample were measured in magnetic fields *H* up to 5 T at temperatures of 2, 5 and 10 K as shown in Fig. 11. In agreement with the temperature dependent susceptibility data, the asymptotic saturation value of the magnetization at 10 K and lower, determined with a Brillouin function, shows only 1/3 of the expected value for a Cu^{2+} spin due to the antiferromagnetic interactions between the spins.

Like previously the magnetic behavior was modelled with the same approach as **Cu(ta)$_2$** (see Fig. S9) using the program PHI [22]. Leading

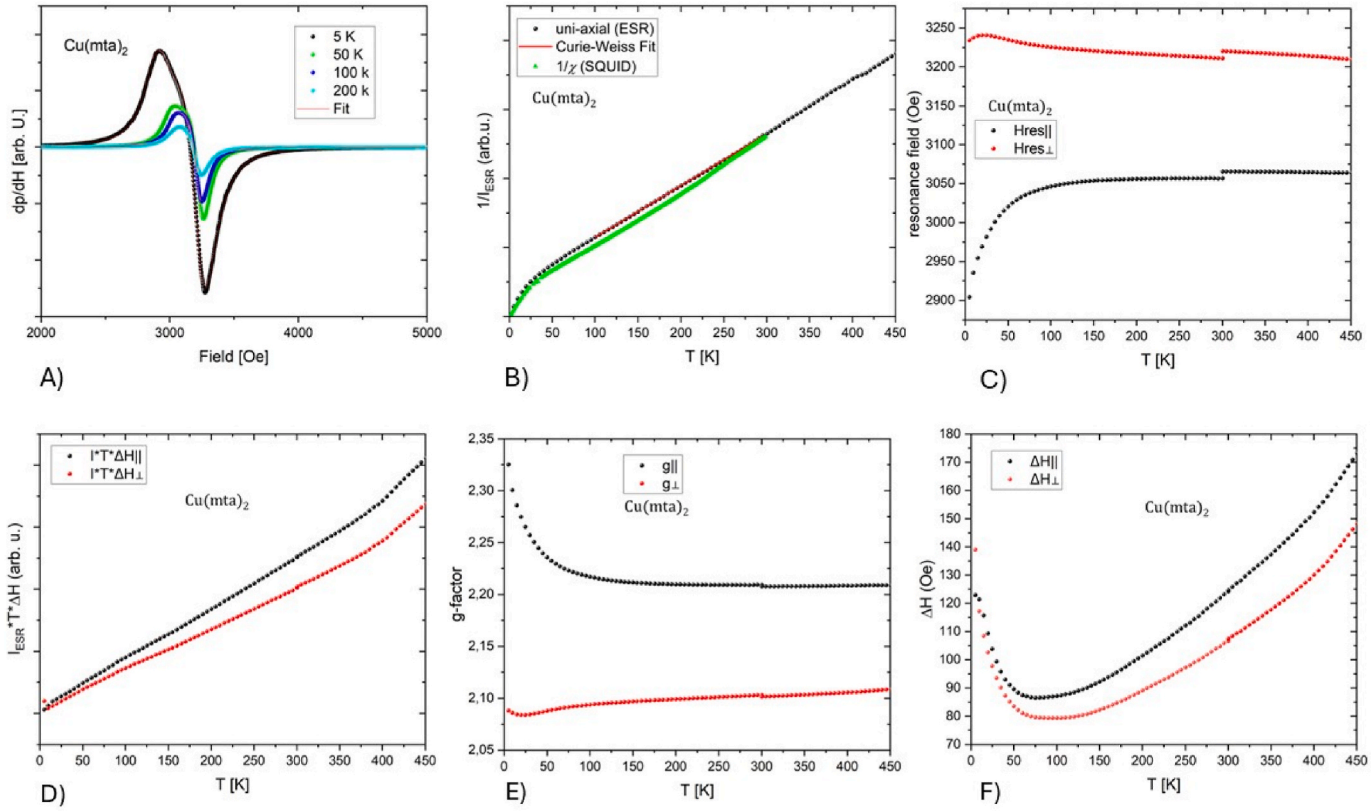

Fig. 9. A) ESR spectra (X-band, 9.48 GHz) of **Cu(mta)$_2$**, closed symbols show the experimental data at 5 K red solid lines represent the uni-axial fit. B) Inverse ESR intensities plotted against temperature. C) Resonance field plotted against temperature. D) The product I_{ESR}•T•ΔH is plotted against temperature. E) Temperature dependence of the g-factor. F) Linewidth ΔH plotted against temperature. (For interpretation of the references to colour in this figure legend, the reader is referred to the Web version of this article.)

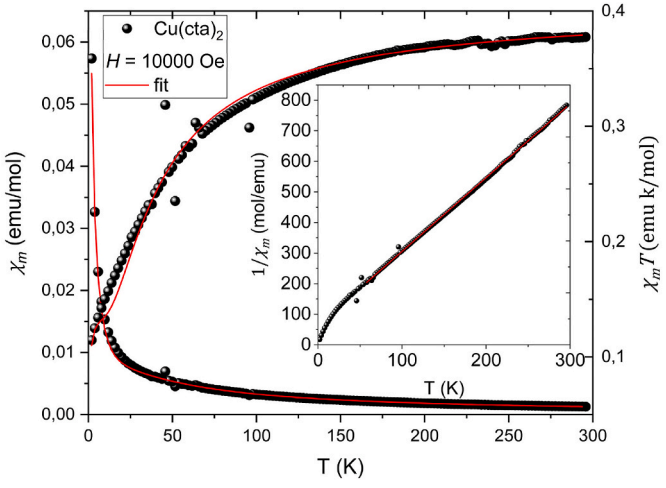

Fig. 10. Temperature dependence of the molar susceptibility χ_m(T) and product χ_mT(T) at 10000 Oe. Open symbols show the experimental data. Red solid lines represent fit 1 based on the Hamiltonian $\widehat{H}_1$ given in the text. Inset: Inverse molar susceptibilities $1/\chi_m$(T) fitted with 1 Ci Weiss law. (For interpretation of the references to colour in this figure legend, the reader is referred to the Web version of this article.)

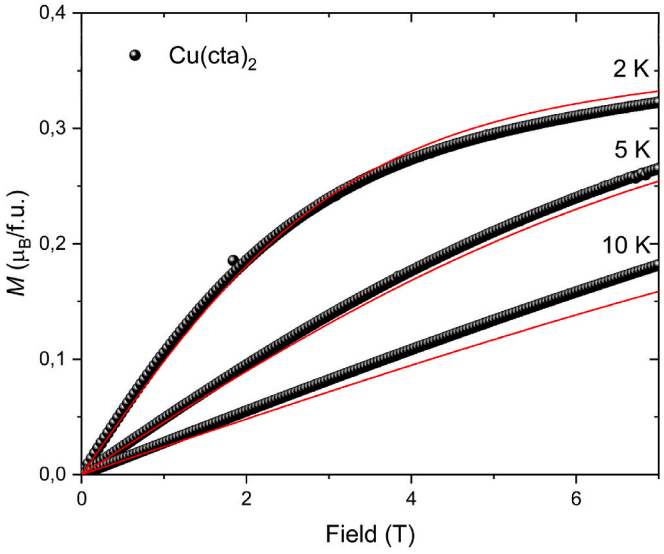

Fig. 11. Field-dependent magnetization curves M(H) at 2, 5 and 10 K. Open symbols show the experimental data, red solid lines represent fit 1 based on the Hamiltonian $\widehat{H}_1$ given in the text. (For interpretation of the references to colour in this figure legend, the reader is referred to the Web version of this article.)

to $J_1/k_B = -19.0(5)$ K, $J_2/k_B = -17.9(5)$ K, $g_1 = 2.46$, $g_2 = g_3 = 1.87$.

This means that the g-factor of the central Cu^{2+} spin S_1 in a stretched octahedral environment is significantly higher at $g_1 = 2.46$, while for the peripheral Cu^{2+} spins S_2 and S_3 in a compressed octahedral environment it is lower than the value of the free electron at $g_2 = 1.87$. The resulting average g-factor of $g = 2.06$ is still in good agreement with the value of $g = 2$ determined from the Curie-Weiss law. All exchange interactions are nearly equivalent, suggesting a random valence bond ground state again evolving a plateau at 1/3 saturation magnetization.

Finally powder ESR measurements were performed up to 300 K on

the same device as for the **Cu(ta)$_2$**. It was noticeable that it makes a significant difference in behavior whether the sample was previously pressed or measured as a powder. Therefore, both measurements are presented.

The ESR spectra at 5 K, 50 K, 100 K and 200 K are illustrated in Fig. 12. The data shown is fitted using a single Lorentzian line, because the signal shape does not indicate the characteristics of a powder pattern. As expected, the inverse intensity $1/I_{ESR}(T)$ determined from the ESR measurements is consistent with the susceptibility from SQUID measurement, as seen in Fig. 12. Here, the scaling factor depends on the measurement settings and only the proportionality was checked. The fitting of the ESR data was performed using a Curie -Weiss-law leading to Curie-Weiss temperatures of $\theta_{CW} = -26$ K for loose powder and $\theta_{CW} = -13$K for the pressed sample. At room temperature *g*-factors of 2.14(2) are found which is in good agreement to the average of the SQUID measurements. A slight influence of the temperature on the g-factors can be observed, starting from 2.15(2) at room temperature, decreasing down to 2.12(2) at 80 K and then increasing again up to 2.15(2) for 1.8 K. This increase towards lower temperatures is probably due to the increase of g-parallel on slowing down of the dynamic Jahn-Teller effect on decreasing temperature.

Both samples start at 5 K with a line width of about 300 Oe and level off at 300 K at about 730 Oe. The slope of the "first step" is approximately the same. The temperature dependence has been evaluated in terms of an Arrhenius behavior:

$$\Delta H = H_0 + A^* e^{\left(-\frac{D}{T}\right)} \quad (2)$$

The corresponding "excitation gap" which can be ascribed to the onset of dynamic Jahn-Teller effect amounts to D = 24 K (powder) and 34 K (pressed), which is within the range of error since there is no sharp transition. The second broader step of the unpressed sample cannot be fitted with the same function. This could be due to the fact that the upper transition is even more blurred and merges into the first one. If the line width is divided into the two transitions as shown in Fig. 13, the transitions have an approximate intensity ratio of two to one, which can be interpreted as transitions of the two different copper sites, whose ratio is also two to one. Squeezing suppresses the transition of one copper site and thus obliterates/mixes with the transition of the other two copper sites.

3.3.4. *Comparison and evaluation*

The three investigated MOFs exhibit antiferromagnetic behavior with notable differences in coupling strength, anisotropy, and temperature dependence of the g-factors. **Cu(ta)$_2$** shows the strongest magnetic interactions, with exchange constants $J_1/k_B = -23.8(5)$ K, $J_2/k_B = -36.8(5)$ K, a Curie-Weiss temperature of $\theta_{CW} = -45$ K (ESR: −72 K), and a Curie constant of 0.42 emu mol^{-1} K. **Cu(mta)$_2$** exhibits similar characteristics ($J_1/k_B = -15.8(5)$ K, $J_2/k_B = -38.8(5)$ K, $\theta_{CW} = -50$ K; ESR: −52 K; C = 0.49 emu mol^{-1} K), with a slightly weaker J_1 interaction.

Cu(cta)$_2$ differs significantly, featuring nearly identical but weaker magnetic couplings ($J_1/k_B = -19.0(5)$ K, $J_2/k_B = -17.9(5)$ K), a lower Curie-Weiss temperature ($\theta_{CW} = -24$ K; ESR: Powder −26 K or Pressed −13 K), and a Curie constant of 0.41 emu mol^{-1} K.

The g-factors of **Cu(ta)$_2$** and **Cu(mta)$_2$** determined from the ESR powder pattern show a significant g anisotropy with moderate temperature dependence: $g_{||}$ increases from ~2.22(2) at room temperature up to 2.34(2) at low temperatures, while $g^{\perp}$ slightly decreases from 2.12(2) and~2.1(2) to 2.10(2) and ~2.08(2). In contrast, **Cu(cta)$_2$** exhibits only a single isotropic g value of about 2.14 with a weak but no significant temperature dependence in the ESR spectra.

All three systems drop to 0.15 emu K/mol around 10 K which

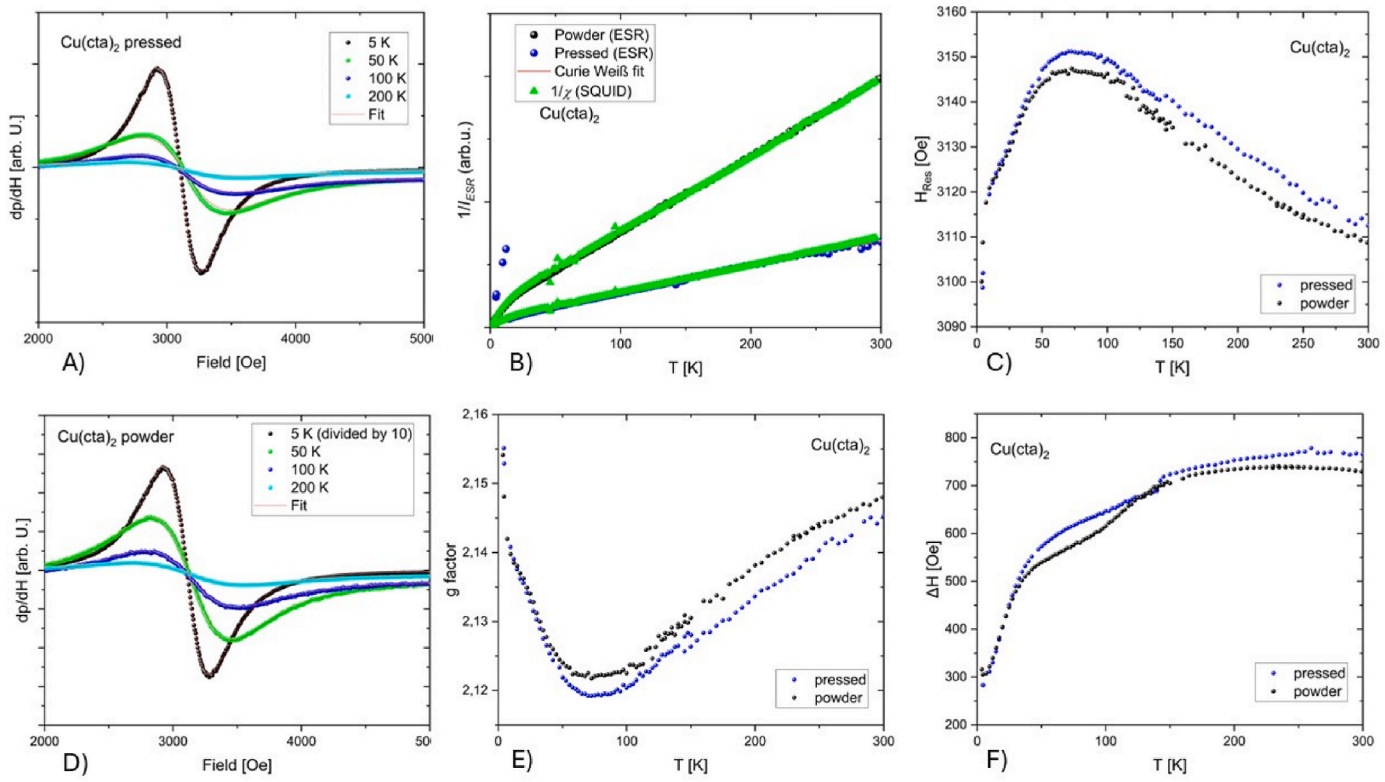

Fig. 12. A) ESR spectra (X-band, 9.48 GHz) of **Cu(cta)$_2$ pressed**, closed symbols show the experimental data at 5 K red solid lines represent the uni-axial fit. B) Inverse ESR intensities plotted against temperature. C) Resonance field plotted against temperature. D) ESR spectra (X-band, 9.48 GHz) of **Cu(cta)$_2$ powder**. E) Temperature dependence of the g-factor. F) Linewidth ΔH plotted against temperature. (For interpretation of the references to colour in this figure legend, the reader is referred to the Web version of this article.)

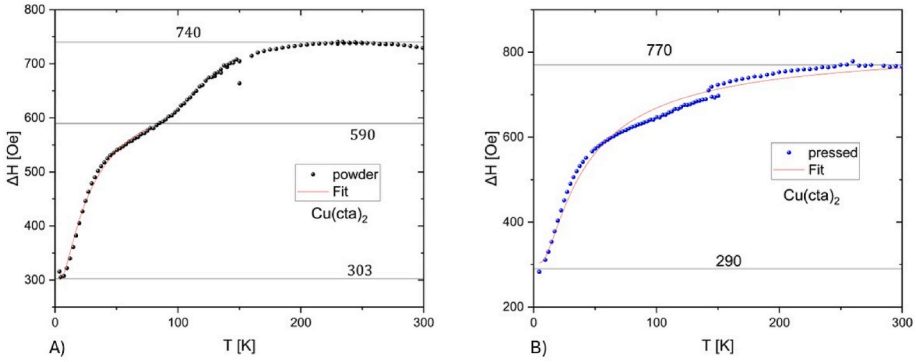

Fig. 13.) Linewidth ΔH plotted against temperature for **Cu(cta)$_2$** powder (a) and pressed (b). The black lines are guides for the eyes to enhance the visibility of the similarities and differences; the red lines are Fits with an Arrhenius-function. (For interpretation of the references to colour in this figure legend, the reader is referred to the Web version of this article.)

corresponds to 1 uncoupled S = ½ spin per copper triangle. This can also be seen in all magnetization measurements and indicates frustration effects.

Combining the magnetic findings with the structural data, a clear correlation emerges between the observed magnetic anisotropy and the coordination environment of the Cu^{2+} centers. A static Jahn–Teller effect fixes the orbital configuration via a lattice distortion, leading to strongly anisotropic exchange interactions with $J_2 \gg J_1$. In contrast, a dynamic Jahn–Teller effect involves rapid orbital fluctuations, so that the orbital configuration is not uniquely defined and the effective exchange couplings J_1 and J_2 are of comparable magnitude.

In **Cu(ta)$_2$**, significant structural distortion is evident, consistent with the pronounced g-factor anisotropy and the temperature dependence observed in the ESR spectra. A strong Jahn–Teller distortion with onset point 400 K can be seen in the ESR data. The resulting distortion towards lower temperatures is typical for 3 d^9 Cu^{2+} ions in elongated octahedral or square pyramidal coordination environments. The new findings align well with the data presented in the earlier study on **Cu(ta)$_2$** [6].

Similarly, **Cu(mta)$_2$** also exhibits structural distortion, both in terms of bond angles and Cu–ligand distances and shows nearly identical magnetic behavior to **Cu(ta)$_2$**. This supports the presence of a Jahn–-Teller distortion extending throughout the framework, but the site of the distortions switches from Cu2 in **Cu(ta)$_2$** to Cu1 in **Cu(mta)$_2$**. The slightly enhanced effect in **Cu(mta)$_2$** may be attributed to the asymmetry introduced by the methyl group, which could locally amplify the distortion and contribute to the observed anisotropy.

In the case of **Cu(cta)$_2$**, the crystal structure at room temperature is already close to ideal cubic symmetry, with no significant static Jahn–Teller distortion present. This is consistent with the nearly equal magnetic exchange parameters and the only weak temperature dependence in the ESR g-factors.

Upon cooling, hints for the onset of a Jahn-Teller effect emerge in **Cu(cta)$_2$**. The distortion which occurs on the time scale of ESR, i.e. 9 GHz, is site-specific and starts at two different temperatures, depending on the local environment of the Cu^{2+} ions within the framework. Importantly, the onset of these local distortions does not necessarily lead to a cooperative structural phase transition but rather results in a gradual transition (no visible transition in powder XRD). External factors such as mechanical pressure, for example through pressing of the MOF powder, can smear one distortion with the other, due to the introduction of local lattice strain and disorder. (not visible in powder XRD).

Despite the potential for such dynamic effects, low-temperature powder X-ray diffraction (PXRD) measurements did not reveal any structural phase transition, supporting the conclusion that the Jahn–-Teller distortions in **Cu(cta)$_2$** remain dynamic and do not result in a cooperative or static symmetry breaking across the crystal lattice.

4. Conclusions

In this study, three Cu-based metal-organic frameworks **Cu(ta)$_2$**, **Cu(mta)$_2$**, and **Cu(cta)$_2$** were synthesized and characterized to investigate the tuning of Jahn-Teller distortions through steric modifications of triazole ligands. **Cu(ta)$_2$** undergoes a pronounced Jahn-Teller transition, whereas **Cu(mta)$_2$** exhibits a static distortion without a clear phase transition. Both compounds display significant Jahn-Teller distortions and share similar magnetic characteristics, including strong antiferromagnetic interactions (e.g. $J_2/k_B = -36.80$ K) and temperature-dependent g-factor anisotropy, as revealed by SQUID and ESR measurements. The structural asymmetry introduced by the methyl substituent in **Cu(mta)$_2$** likely enhances local disorder, thereby supporting the cooperative Jahn-Teller transition and stabilizing the distorted phase.

In contrast, **Cu(cta)$_2$** crystallizes in an undistorted, near-ideal cubic symmetry with weaker and nearly identical magnetic exchange interactions. While dynamic Jahn-Teller distortions start to slow down upon cooling, no cooperative structural transition was observed via PXRD, suggesting that the steric bulk of the cta ligand partially suppresses but does not eliminate local distortions. External pressure further smears site-specific transitions, indicating sensitivity to mechanical strain. The dynamic freezing may serve as an indicator for quantum spin-liquid behavior, which has been proposed for materials such as Mn(ta)$_2$ [9], where conventional magnetic ordering is suppressed even at low temperatures.

Overall, while steric ligand modification in **Cu(cta)$_2$** mitigates the static Jahn-Teller effect, complete suppression is not achieved. These findings demonstrate that tuning structural rigidity through ligand design can modulate magnetic anisotropy and distortion phenomena in Cu-based MOFs, providing a pathway for tailoring multifunctional properties in such frameworks.

This work was supported by the Deutsche Forschungsgemeinschaft (DFG, German Research Foundation) via TRR 360-project no. 492547816 (Augsburg, Munich, Stuttgart, Lepzig), SFB 1143.

CRediT authorship contribution statement

Marcel Hirrle: Writing – original draft, Investigation. **Richard Röß-Ohlenroth:** Writing – review & editing, Investigation. **Stephan Reschke:** Investigation. **Björn Bredenkötter:** Investigation. **Hans-Albrecht Krug von Nidda:** Writing – review & editing, Formal analysis. **Dirk Volkmer:** Supervision.

Declaration of competing interest

The authors declare that they have no known competing financial interests or personal relationships that could have appeared to influence

the work reported in this paper.

Appendix A. Supplementary data

Supplementary data to this article can be found online at https://doi.org/10.1016/j.jpcs.2026.113566.

Data availability

Data will be made available on request.

References

[1] A.E. Thorarinsdottir, T.D. Harris, Chem. Rev. 120 (2020) 8716, https://doi.org/10.1021/acs.chemrev.9b00666.

[2] C. Yang, R. Dong, M. Wang, P.S. Petkov, Z. Zhang, M. Wang, P. Han, M. Ballabio, S. A. Bräuninger, Z. Liao, et al., Nat. Commun. 10 (2019) 3260, https://doi.org/10.1038/s41467-019-11267-w.

[3] a) R. Dong, Z. Zhang, D.C. Tranca, S. Zhou, M. Wang, P. Adler, Z. Liao, F. Liu, Y. Sun, W. Shi, et al., Nat. Commun. 9 (2018) 2637, https://doi.org/10.1038/s41467-018-05141-4;
b) K.-B. Wang, Q. Xun, Q. Zhang, EnergyChem 2 (2020) 100025, https://doi.org/10.1016/j.enchem.2019.100025;
c) K. Wang, Y. Guo, Q. Zhang, Small Struct. 3 (2022), https://doi.org/10.1002/sstr.202100115;
d) K. Wang, C. Chen, Y. Li, Y. Hong, H. Wu, C. Zhang, Q. Zhang, Small 19 (2023) e2300054, https://doi.org/10.1002/smll.202300054.

[4] a) J.F. Nossa, M.F. Islam, M.R. Pederson, C.M. Canali, Phys. Rev. B 107 (2023), https://doi.org/10.1103/PhysRevB.107.245402;
b) B. Kintzel, M. Böhme, J. Liu, A. Burkhardt, J. Mrozek, A. Buchholz, A. Ardavan, W. Plass, Chem. Commun. (Cambridge, England) 54 (2018) 12934, https://doi.org/10.1039/C8CC06741D.

[5] a) M.-H. Zeng, Z. Yin, Y.-X. Tan, W.-X. Zhang, Y.-P. He, M. Kurmoo, J. Am. Chem. Soc. 136 (2014) 4680, https://doi.org/10.1021/ja500191r;
b) X. Zhao, S. Liu, Z. Tang, H. Niu, Y. Cai, W. Meng, F. Wu, J.P. Giesy, Sci. Rep. 5 (2015) 11849, https://doi.org/10.1038/srep11849.

[6] M. Grzywa, D. Denysenko, J. Hanss, E.-W. Scheidt, W. Scherer, M. Weil, D. Volkmer, Dalton Trans. 41 (2012) 4239, https://doi.org/10.1039/C2DT12311H.

[7] S. Biswas, M. Tonigold, M. Speldrich, P. Kögerler, M. Weil, D. Volkmer, Inorg. Chem. 49 (2010) 7424, https://doi.org/10.1021/ic100749k.

[8] M. Grzywa, R. Röß-Ohlenroth, C. Muschielok, H. Oberhofer, A. Błachowski, J. Żukrowski, D. Vieweg, H.-A.K. von Nidda, D. Volkmer, Inorg. Chem. 59 (2020) 10501, https://doi.org/10.1021/acs.inorgchem.0c00814.

[9] R.P. Nutakki, R. Röß-Ohlenroth, D. Volkmer, A. Jesche, H.-A.K. von Nidda, A. A. Tsirlin, P. Gegenwart, L. Pollet, L.D.C. Jaubert, Phys. Rev. Res. 5 (2023), https://doi.org/10.1103/PhysRevResearch.5.L022018.

[10] J.G. Park, B.A. Collins, L.E. Darago, T. Runčevski, M.E. Ziebel, M.L. Aubrey, H.Z. H. Jiang, E. Velasquez, M.A. Green, J.D. Goodpaster, et al., Nat. Chem. 13 (2021) 594, https://doi.org/10.1038/s41557-021-00666-6.

[11] S.M. Kronawitter, R. Röß-Ohlenroth, S.A. Hallweger, M. Hirrle, H.-A. Krug von Nidda, T. Luxenhofer, E. Myatt, J. Pitcairn, M.J. Cliffe, D. Daisenberger, et al., J. Mater. Chem. C 12 (2024) 4954, https://doi.org/10.1039/D4TC00360H.

[12] M. Hirrle, R. Röß-Ohlenroth, T. Luxenhofer, B. Bredenkötter, M. Kraft, H.-A. Krug von Nidda, D. Volkmer, J. Solid State Chem. 348 (2025) 125328, https://doi.org/10.1016/j.jssc.2025.125328.

[13] K.I. Kugel, D.I. Khomskiĭ, Sov. Phys. Usp. 25 (1982) 231, https://doi.org/10.1070/PU1982v025n04ABEH004537.

[14] Proc. R. Soc. Lond A 161 (1937) 220, https://doi.org/10.1098/rspa.1937.0142.

[15] J. Thomas, S. Jana, S. Liekens, W. Dehaen, Chem. Commun. (Cambridge, England) 52 (2016) 9236, https://doi.org/10.1039/C6CC03744E.

[16] Bruker, *APEX4*, Bruker.

[17] Saint Madison, Bruker Analytical X-Ray Systems, INC., 2021.

[18] L. Krause, R. Herbst-Irmer, G.M. Sheldrick, D. Stalke, J. Appl. Crystallogr. 48 (2015) 3, https://doi.org/10.1107/S1600576714022985.

[19] Sheldrick, SHELXL-2019/1, 2019.

[20] A.L. Spek, Acta Crystallogr. D 65 (2009) 148, https://doi.org/10.1107/S090744490804362X.

[21] A. Abragam, B. Bleaney, Electron Paramagnetic Resonance of Transition Ions, Oxford Univ. Press, Oxford, 2013.

[22] N.F. Chilton, R.P. Anderson, L.D. Turner, A. Soncini, K.S. Murray, J. Comput. Chem. 34 (2013) 1164, https://doi.org/10.1002/jcc.23234.

[23] a) T. Moriya, Phys. Rev. Lett. 4 (1960) 228, https://doi.org/10.1103/PhysRevLett.4.228;
b) T. Moriya, Phys. Rev. 120 (1960) 91, https://doi.org/10.1103/PhysRev.120.91.

[24] D.L. Huber, M.S. Seehra, J. Phys. Chem. Solid. 36 (1975) 723, https://doi.org/10.1016/0022-3697(75)90094-3.